MNRAS (2017)
Advance Access publication 2017 January 15
doi:10.1093/mnras/stx092

Diagnostics of circumstellar grains in geometric models – I. Structure and composition

J. H. P. Dawes[1]★ and J. S. Greaves[2]

[1]*Department of Mathematical Sciences, University of Bath, Claverton Down, Bath BA2 7AY, UK*
[2]*School of Physics and Astronomy, Cardiff University, Queen's Buildings, The Parade, Cardiff CF24 3AA, UK*

Accepted 2017 January 12. Received 2017 January 7; in original form 2016 April 22

ABSTRACT

The spectral energy distribution (SED) of circumstellar dust has been extensively used to diagnose the sizes and compositions of dust grains. We show that variations of SED slope in the long-wavelength (submillimetre to radio) regime can be used to diagnose the gross physical nature (and hence origins) of the dust, using simple geometric models that complement the use of detailed simulations. We consider two dust grain types: (i) clustered aggregates of smaller particles (monomers) and (ii) composite grains comprising ferrous inclusions within a silicate matrix. These types are intended to be analogous to fluffy cometary particles and fragments of compacted asteroids, respectively. Our results indicate that clusters of silicate grains produce a smooth SED, while composite grains with FeS inclusions produce an SED that has a pronounced drop at a wavelength an order of magnitude larger than the grain size, and is flatter at long wavelengths. As a test case, we compare the model predictions to flux measurements of the TW Hydrae disc. This SED shows a drop that only occurs in our models of compacted grains with inclusions. Since the TW Hya discs span approximately 10–40 au in radius, fluffy particles from comets were perhaps expected, as in the Sun's Kuiper belt.

Key words: protoplanetary discs – circumstellar matter – submillimetre: planetary systems.

1 INTRODUCTION

The processes of assembling and breaking dust grains are important for understanding planetary systems. Small sub-μm dust is incorporated from the interstellar medium into the circumstellar disc, which surrounds a protostar, and from which the pre-main-sequence star then develops by accretion. The dense disc environment promotes grain sticking up to about mm-sizes, but laboratory experiments have shown a barrier above this, as collisions of mm-particles tend to result in fragmentation. Processes that could boost growth include embedding, sticking of icy surfaces and electrical attraction (e.g. Blum 2010). However nature actually overcomes this barrier, further growth to 'pebbles', 'boulders', etc., should eventually build planetesimals and planetary cores, particularly if assisted by turbulence and gravitational focusing to increase collision rates (e.g. Ormel & Okuzumi 2013).

Aggregation of grains through collisions relies to some extent on their velocities being moderated by the viscous drag of gas in the disc. When the gas disperses, a second generation of dust results from the unmoderated collisions of planetesimals, forming 'debris' discs that persist around stars of ages comparable to the Sun. The dispersal of gas is mainly complete by about 10 Myr, but can have varying time-scales at different radii and heights in the disc, relating to the penetration of stellar photons, impact of stellar particle wind and shielding by forward gas layers, among other effects (e.g. Woitke 2016). Hence, the aggregation and fragmentation of particles can actually occur at the same time (see Birnstiel, Dullemond & Pinilla 2013), and the evolutionary track is difficult to follow.

Understanding the emission properties of grains can thus give important clues to the emergence of a planetary system. For example, if grains have not grown far by around 10 Myr, planetesimals may not be constructed at all. If the size distribution of debris follows a collisional cascade, the total numbers of parent colliders may be estimated, and compared, for example, to those around the Sun (Greaves et al. 2012). If the emission is found to be characteristic of icy or iron particles, the parent bodies can also be classified as similar to the Sun's Kuiper belt of comets, or its asteroid belt of more differentiated objects (Lisse et al. 2012).

1.1 Approaches to grain physics

Much of our data is from photometric measurements of discs. Imaging has just started to benefit from interferometry at millimetre and radio wavelengths, so that regions in which grains are coagulating or fragmenting can be found essentially by image analysis (e.g. Pérez et al. 2012). These wavebands are also rather optically

★ E-mail: J.H.P.Dawes@bath.ac.uk

thin, getting around the hazards of interpreting image data from the optical and infrared, where not all photons emerge from the disc, as they undergo re-absorption and scattering. However, where only long-wavelength photometry is available, solutions to the state of the disc can be highly degenerate. For example, the same flux could be produced regardless of how much the grains have settled to the mid-plane, and this factor affects the mass budget available to form planetary cores in or near this plane.

In this paper, we consider what can be inferred about grains from interpreting photometric measurements over a range of wavelengths, i.e. the spectral energy distribution (SED) of the disc. We are interested in establishing simple diagnostics of the nature of the particles, and we focus on two issues: whether they are solid or porous, and their composition. Spectral information in the infrared allows small particles to be identified as crystalline or amorphous, by looking for a characteristic 'bump' in the SED at a wavelength of 10 μm (e.g. Min et al. 2007). However, the long-wavelength side of the SED is relatively featureless, and so the challenge is to relate grain properties to the overall shape of the SED, in particular any changes of slope. Previous work has looked, for example, at the porosity of debris and its effect on the SED (e.g. Booth et al. 2010; Sheret, Dent & Wyatt 2004), and the size distribution as it extends to the centimetre regime (Greaves et al. 2012).

Realistic studies rapidly become computationally expensive when detailed grain physics is used. For example, Min et al. (2013) present results for aggregates of many small spheres (monomers), similar to interplanetary dust particles recovered from the stratosphere. The absorption and emission of the spheres is handled by Mie theory, while the discrete dipole approximation is used for the aggregate, generated as a Gaussian random field object (see, for other approaches, Shen, Draine & Johnson 2008). These calculations can model particular data sets very well, but are not readily adaptable to a new disc without lengthy rerunning of a suite of models.

Our aim here, in contrast, is to test whether analytical methods can be speedily applied to an ensemble of discs. The approach is similar to that recently applied by Cuzzi, Estrada & Davis (2014) to model SEDs for small aggregates of particles in planetary and stellar atmospheres. In our example scenarios, we test how feasible it is to distinguish between cometary and asteroidal origins, for large grains, considering the former as loose aggregated clusters and the latter as solid rock with inclusions of other minerals. We follow simple model cases that bring out the main features of our approach. The grains have a single size, and are placed at a single distance from a Sun-like star, in quantities similar to the median value of real circumstellar discs of T Tauri stars (e.g. Henning et al. 1993). The properties varied are porosity and the nature of inclusions (of dielectric minerals). The effective particle areas for the absorption of starlight and reemission of longer wavelengths are calculated, and the balance of energy absorbed and emitted sets the grain temperature. The emitted flux is then calculated as a function of wavelength, in regimes smaller, larger and similar to particle size, forming an SED. Finally, the suite of SEDs is compared to an example data set across two decades of frequency, to assess whether the disc contains dust that is cometary or asteroidal.

The organization of the paper is as follows. Section 2 summarizes the physical attributes of dust grains that provide the foundation for our model. Section 3 presents our results: the SED for different shapes and compositions of dust grains. In Section 4, we compare these results with observational data. Section 5 concludes and describes directions for future work.

2 PHYSICS OF DUST GRAINS

In this section, we discuss the physical characteristics that are key to our model. First, we consider the geometry of the dust grains: more precisely their effective surface areas over which absorption and emission take place, at relevant wavelengths. Then, along with a consideration of their material composition, we discuss the reflectivity, dielectric constants, and absorption and emission characteristics of the grains. The relative sizes of the grains, and of their constituent monomers or inclusions, need to be compared with the relevant radiation wavelengths in order to apply the correct absorption and emission characteristics.

2.1 Shape

Shape plays a key role due to our need to consider both absorption and emission processes, and these involve different surface areas and different wavelength regimes. Broadly speaking, dust grains absorb radiation only over the projection of their cross-sectional area on to a plane orthogonal to the direction of the radiation incident from the star, which we denote by $A_{\rm eff}$. However, dust grains emit radiation over their entire surface area $A_{\rm total}$. For a solid convex body, there is a well-known geometric relation between these two areas, taking the average over all grain orientations: The average projected cross-sectional area (where the average is taken over all directions of incident radiation) $A_{\rm eff} = \frac{1}{4}A_{\rm total}$. The proof of this result goes back to Cauchy and can be found, for example, in the appendix to Hildebrand (1983). For non-convex bodies, there is no simple extension of this result, and we resort to an estimate for a simple geometry that enables us to test the sensitivity of this factor of $\frac{1}{4}$ to changes in shape. Specifically, we consider the following two contrasting shapes of dust grains:

(i) Clustered aggregates of monomers: Here, we consider a collection of small monomers clustered together in an irregular manner that forms a 'fluffy' overall shape within which the material occupies only a small fraction of the volume enclosed by its convex hull, i.e. a relatively low volume fraction.

(ii) Compacted object with inclusions: In this case, we consider a solid silicate spherical grain that contains smaller metallic inclusions, again at a low volume fraction. The combination of metallic and silicate components gives rise to a change in the effective dielectric coefficient $\epsilon_{\rm eff}$ as we discuss below.

We now discuss the geometry of the different models for dust grains in turn.

2.1.1 *Clustered aggregates of monomers*

For cometary dust, we consider the dust to be aggregates of smaller grains (monomers), as found in interplanetary dust particles recovered in the stratosphere. Similarly, dust observed around comets is fluffy, silicate-rich and inferred to have sizes from 0.1 μm up to nearly a millimetre (Niimi et al. 2012; de Val-Borro et al. 2014). We identify this lower bound as the size of our monomers, as it is also near the top end for small interstellar particles from which the aggregates build up in the disc environment. We set the representative radius r of the aggregate to be 1 mm and the radius of monomers to be $\delta = 100$ nm, i.e. $\delta \ll r$. For these parameters, the emitted far-infrared to centimetre waves span a range from smaller to larger than the aggregate. Monomers that are of the order of 0.1 μm in radius are approximately in the geometric optics regime, given our use later, in Section 2.3, of wavelengths of incident radiation $\lambda \sim 2\pi\delta \sim 0.5\,\mu$m.

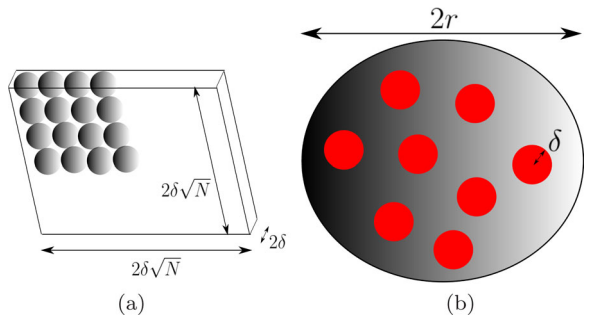

Figure 1. Two possible idealized geometries for dust grains. (a) A clustered aggregate formed from $N \gg 1$ monomers of radius δ producing a cluster of length-scale $r \gg \delta$. (b) A 'compacted' composite grain model: a large silicate grain of radius r containing inclusions of radius $\delta \ll r$ consisting of iron sulphide.

The complex geometry of the aggregate will in general result in neighbouring monomers obscuring each other, hence affecting the efficiency of both absorption and emission of radiation. We content ourselves here with a simplified model that captures a low level of obscuration.

The central point of any such geometric calculation is to estimate the ratio $A_{\rm eff}/A_{\rm total}$ due to the blocking and non-convexity of the cluster overall. Non-convexity implies that the reduction in the average area for absorption is expected to be larger than the drop in the total area over which emission to the open sky is possible. To see this, consider points near the centre of a large concave region: They are always able to emit to the open sky but are only rarely able to directly absorb radiation from the central star. It is not clear from this qualitative argument whether a suitable value for the ratio $A_{\rm eff}/A_{\rm total}$ is slightly less than 1/4, or reduced by orders of magnitude. Therefore, we consider specific configurations in order to estimate a suitable value for $A_{\rm eff}/A_{\rm total}$.

For emission we take the optimal case, in that we envisage an 'open' well-spread-out cluster in which neighbouring spherical monomers do not influence the ability of each other to radiate to the open sky. The overall volume fraction of solid inclusions within an overall spherical convex hull is denoted f since in this case the 'inclusions' are the solid material and the 'external matrix' is empty space. We note that f should not be taken to exceed $\pi/(3\sqrt{2}) \approx 0.74$ since this is the optimal density for packing spheres (achieved by hexagonal close packing). In such a configuration, the number N of solid inclusions in the cluster can be estimated via

$$\frac{4}{3}\pi\delta^3 N = \frac{4}{3}\pi r^3 f \Rightarrow N = f(r/\delta)^3 \gg 1.$$

The (maximum) total surface area over which emission takes place is clearly

$$A_{\rm total} = 4\pi\delta^2 N \equiv 4\pi\delta^2 f(r/\delta)^3 = 4\pi f r^3/\delta,$$

assuming that every spherical inclusion can radiate openly over its full surface area.

The total effective surface area for absorption is more difficult to estimate since we wish to take obscuration into account. If we were to treat all monomers as independent and not obscuring each other, we would end up purely with the Cauchy result that $A_{\rm eff}/A_{\rm total} = 1/4$. To take obscuration into account while maintaining the validity of our result above in which every spherical inclusion is able to radiate energy to the open sky rather than to each other, we consider a configuration of monomers in which they all lie within a 2D slab that is one monomer thick; see Fig. 1(b).

Such a slab can be viewed approximately as a convex body having dimensions roughly $2\delta\sqrt{N} \times 2\delta\sqrt{N} \times 2\delta$. The total surface area of the convex slab is therefore twice the sum of the pairwise products of these dimensions, i.e. $A_{\rm slab} = 2(2\delta\sqrt{N})^2 + 2 \times 2\delta\sqrt{N} \times 2\delta + 2 \times 2\delta\sqrt{N} \times 2\delta = 8\delta^2 N + 16\delta^2\sqrt{N}$. Considering the slab as a convex body implies that we can estimate its average projected area to be $A_{\rm slab}/4$, i.e.

$$A_{\rm eff} = 2\delta^2 N + 4\delta^2\sqrt{N} = 2fr^2/\delta + 4f^{1/2}r^{3/2}\delta^{1/2}.$$

We therefore obtain

$$\frac{A_{\rm eff}}{A_{\rm total}} = \frac{2\delta^2 N + 4\delta^2\sqrt{N}}{4\pi\delta^2 N} = \frac{1}{2\pi} + \frac{1}{\pi\sqrt{N}} \approx \frac{1}{2\pi} \text{ when } N \gg 1.$$

Thus, the ratio $A_{\rm eff}/A_{\rm total}$ drops from 1/4 but only to around 1/6 as a result of the blocking of absorption of particles by their neighbours in the slab configuration.

It is interesting to note that, with the assumptions made above, the ratio $A_{\rm eff}/A_{\rm total}$ depends only on the number of monomers N per dust grain rather than depending separately on δ and f.

2.1.2 Compacted object with inclusions

The asteroidal dust case is based on micrometeorites, with a silicate matrix containing iron sulphide inclusions. This has especially interesting optical properties, but pure iron inclusions are also found in nature. A discussion is presented by Duprat et al. (2007), who recovered rather pristine particles that had fallen into snow in Antarctica. These were up to a millimetre in size, with inclusions reaching around 10 μm in the interior of the meteorite. We adopt these two sizes here, for r and δ, respectively. Note that the inclusion size is different from that taken for the monomers in the clustered aggregate case above, while the representative radius $r = 1$ mm is taken to be the same. This facilitates comparison, although meteorites can also be much larger and contain bigger sub-elements (e.g. millimetre-sized calcium–aluminium-rich inclusions).

The asteroidal case, illustrated in Fig. 1(b), enables us to explore the dependence of the SED on composition rather than geometry. The incorporation of iron sulphite inclusions within a silicate matrix demands that we use an effective medium approximation (EMA; equation 1) to derive an expression for the overall dielectric constant; these distinct materials have dielectric coefficients that show opposite dependencies on wavelength (see Fig. 2). However, we deal only with the simplest geometry in this case, and assume that the expressions for $A_{\rm eff}$ and $A_{\rm total}$ are simply those for a solid sphere of radius r, as shown in Table 1.

2.2 Dielectric coefficients

Since we wish to consider small dust grains that are composites, it is necessary to estimate the overall (complex-valued) dielectric coefficient of a composite grain. The complex value of the dielectric constant ϵ (for a single material) is the square root of its complex refractive index. Hence, the optical properties of our materials are now fully described, but where photons interact with the composite, suitable averaged properties are needed.

A straightforward approach to this is via an EMA; see Bohren & Huffman (1983). Consider the general case of a grain composed of a basic 'matrix' with dielectric function $\epsilon_{\rm m}$, which comprises a fraction $1 - f$ of the volume, together with spherical inclusions of a different material with dielectric function ϵ, which comprises the remaining volume fraction f.

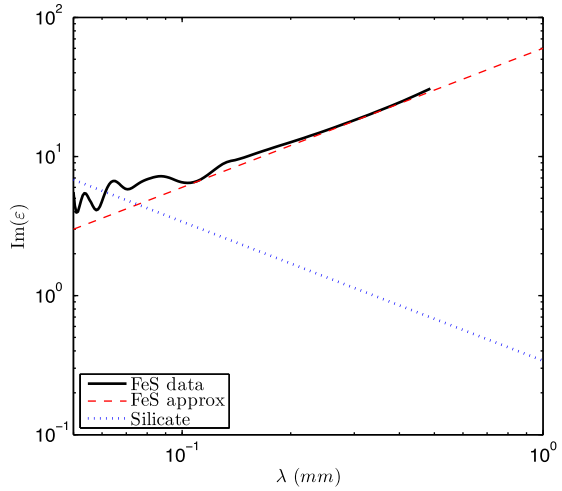

Figure 2. Experimental data for the imaginary part of the dielectric coefficient $\mathrm{Im}(\epsilon)$ for iron sulphide FeS (black solid line), from Henning & Mutschke (1997), together with the approximation (red dashed line) $\mathrm{Im}(\epsilon_{\mathrm{FeS}}) = 6.0 \times 10^4 \lambda$ (where λ is measured in metres). We also show the dependence on λ of the imaginary part of the dielectric coefficient for astronomical silicate $\mathrm{Im}(\epsilon_{\mathrm{sil}})$; see equation (2).

The most straightforward EMA is the Maxwell Garnett mixing rule, which gives the following explicit formula for the effective dielectric coefficient ϵ_{eff}:

$$\epsilon_{\mathrm{eff}} := \frac{(1-f)\epsilon_{\mathrm{m}} + f\beta\epsilon}{1-f+f\beta},$$

where $\beta := 3\epsilon_{\mathrm{m}}/(\epsilon + 2\epsilon_{\mathrm{m}})$. However, the Maxwell Garnett formula is usually taken to be valid only when the inclusions occupy only a very small fraction of the material. In this paper, we use the more complicated Bruggemann formula, which is a more general EMA, in the sense that it is not restricted to cases where the volume fraction f of inclusions is small; that is, interactions between inclusions are accounted for. In our situation, Bruggemann's expression for the effective dielectric coefficient ϵ_{eff} is given by solving the expression

$$(1-f)\frac{\epsilon_{\mathrm{m}} - \epsilon_{\mathrm{eff}}}{\epsilon_{\mathrm{m}} + 2\epsilon_{\mathrm{eff}}} + f\frac{\epsilon - \epsilon_{\mathrm{eff}}}{\epsilon + 2\epsilon_{\mathrm{eff}}} = 0. \quad (1)$$

This can be rearranged to yield a quadratic equation for ϵ_{eff}. At small f, the relevant root of this quadratic expression converges to the Maxwell Garnett mixing rule.

When either the matrix or the inclusions are actually vacuum, we set the relevant dielectric coefficient $\epsilon = 1$. In general, dielectric coefficients are complex-valued, and they vary with the wavelength λ of the incident radiation. A useful dimensionless ratio is $x := 2\pi a_{\mathrm{eff}}/\lambda$, where a_{eff} is the typical radius of a dust grain.

In the small particle limit $x \ll 1$, the efficiency of absorption of a particle with dielectric coefficient ϵ surrounded by material with dielectric coefficient ϵ_{m} is given by the quantity $Q^{\mathrm{abs}}(\lambda) := 4x\mathrm{Im}(\alpha(\lambda))$, which depends on the function $\alpha(\lambda)$, which is, in turn, defined in terms of the dielectric coefficients as follows:

$$\alpha(\lambda) := \frac{\epsilon - \epsilon_{\mathrm{m}}}{\epsilon + 2\epsilon_{\mathrm{m}}},$$

where $\epsilon \equiv \epsilon_{\mathrm{eff}}$ and $\epsilon_{\mathrm{m}} = 1$ for a (composite) dust grain in the middle of the ISM. In the situations we investigate here, however, we find that we do not remain in the small particle limit and so need to compute $Q^{\mathrm{abs}}(\lambda)$ using the numerically evaluated exact solution provided by Mie theory; see Section 2.4.

In the remainder of this paper, we consider two specific materials: silicate and iron sulphide (FeS). Data suggest that in the long-wavelength regime in which we are particularly interested, the dielectric coefficients ϵ_{sil} and ϵ_{FeS} can be well approximated by the following formulas:

$$\begin{aligned} \epsilon_{\mathrm{sil}} &= 12.0 + 3.4 \times 10^{-4}/\lambda_{\mathrm{i}}, \\ \epsilon_{\mathrm{FeS}} &= 40.0 + 6.0 \times 10^4 \lambda_{\mathrm{i}}, \end{aligned} \quad (2)$$

where λ denotes the wavelength in metres. The real parts of the dielectric coefficients are assumed to be independent of wavelength λ. Fig. 2 shows the experimental data reported by Henning & Mutschke (1997) for iron sulphide, along with the approximation ϵ_{sil} from Draine & Lee (1984) for comparison. Köhler, Jones & Ysard (2014) present recent calculations for interstellar grains with FeS inclusions predicting SEDs up to 1 mm wavelength.

2.3 Absorption and reflectivity

In this section, we discuss how we combine the geometrical and dielectric data from the previous section to compute the SED. We assume throughout this discussion that the disc is optically thin. One might initially assume that all incident stellar photons are absorbed by dust grains, and that all this energy is then reemitted at longer wavelengths. However, some materials have a non-negligible reflectivity in the optical regime, meaning that the incident stellar light is in part scattered and not absorbed. This effective reduction in the absorbed energy is material-dependent, and must be accounted for in the energy balance, as follows. The reflectivity of the material is defined as the proportion of incident photons that is reflected, and is given by

$$\mathcal{R} = \frac{(n_{\mathrm{r}}-1)^2 + n_{\mathrm{i}}^2}{(n_{\mathrm{r}}+1)^2 + n_{\mathrm{i}}^2},$$

where n_{r} and n_{i} are the real and imaginary parts of the complex refractive index n of the material at the relevant wavelength. The absorption coefficient is therefore $\mathcal{A} := 1 - \mathcal{R}$.

Standard values for various materials were tabulated by Pollack et al. (1994), and convenient plots are available in Cuzzi et al. (2014). In the optical regime, we make the assumption that the peak-emission wavelength of around 0.5 μm for a Sun-like star is representative of the incident-light regime. For astronomical silicate, we find that at a wavelength of around 0.5 μm, typical values

Table 1. Volume, areas and length-scale in terms of the primary free parameters that describe each class of shapes. $\ell = L/r$ is the particle aspect ratio, r is a length-scale of the convex hull of the shape, δ is the size of the inclusions (note that implicitly $\delta \ll r$) and f is the volume fraction of included material.

Name	Free parameters	V	Absorption: A_{eff}	Emission: A_{total}
Clustered aggregate	δ, f	$f\frac{4}{3}\pi r^3$	$2fr^3/\delta + 4f^{1/2}r^{3/2}\delta^{1/2}$	$4\pi f r^3/\delta$
Compacted object	δ, f	$\frac{4\pi}{3}r^3$	πr^2	$4\pi r^2$

are $n_r = 1.6$ and $n_i = 2 \times 10^{-4}$. This yields $\mathcal{R} = 0.053$ and hence $\mathcal{A} = 0.947$ (to 3 dp).

For the compacted object model of sparsely distributed FeS inclusions in a silicate sphere, we use the typical values for FeS of $n_r = 2.0$ and $n_i = 2.0$. This yields a reflectivity coefficient for FeS of $\mathcal{R} = 0.385$ (3 dp). To estimate the reflectivity of the dust grain as a whole, we use the geometric argument above to take a linear combination of the reflectivities of the silicate and the FeS, resulting in an absorbancy coefficient of

$$\mathcal{A} = \mathcal{A}_{\rm sil}\left(1 - \frac{\pi}{6} f^{2/3}\right) + \mathcal{A}_{\rm FeS}\frac{\pi}{6} f^{2/3}.$$

This arises from an estimate of the average area of a slice through an inclusion at the surface of the aggregate and their average spacing, given that their total volume fraction is only f. For the typical values indicated above, for a volume fraction $f = 0.1$, we obtain $\mathcal{A} = 0.909$, and for $f = 0.3$, we obtain $\mathcal{A} = 0.869$ (both to 3 dp). These factors $\mathcal{A}$ are included below when we compute the total energy absorbed by the grains.

The standard expression for the total energy E_1 absorbed by the grains is given by

$$E_1 = A_{\rm eff}\, \mathcal{A}\, R_*^2 \int_0^\infty B(\lambda, T_*)\, {\rm d}\lambda,$$

where $B(\lambda, T_*)$ denotes the Planck function

$$B(\lambda, T_*) = \frac{2hc^2}{\lambda^5}\left[\exp\left(\frac{hc}{\lambda k_{\rm B} T_*}\right) - 1\right]^{-1},$$

which describes the distribution of energy emitted by the central object (star) at a temperature T_*, R_* is the radius of the star, h and $k_{\rm B}$ are Planck's and Boltzmann's constants and c is the speed of light in vacuum.

2.4 Emission

Let $T_{\rm grain} \ll T_*$ be the temperature of the dust grains. Since much of this emission occurs in the regime where the wavelength of the emitted radiation is comparable with the size of the dust grain, the emission of radiation from the dust grain is imperfect, with a quality parameter $Q^{\rm abs}(\lambda)$. For this computation, it is essential to resolve the behaviour and compute the material-dependent factor $Q^{\rm abs}(\lambda)$. This computation is a well-known part of Mie theory, and we will not present further mathematical details here.

We used the MATLAB code due to C. Mätzler, which is a direct implementation of the calculations described in Bohren & Huffman (1983). Note that the calculation of $Q^{\rm abs}(\lambda)$ actually demands two input parameters: the size ratio x and the complex refractive index $n = \sqrt{\epsilon_{\rm eff}(\lambda)}$ computed from the effective dielectric coefficient of the material that comes from the Bruggemann formula, so in Equation (3) we show this dependence by writing $Q^{\rm abs}(\lambda)$ as $Q^{\rm abs}(\lambda, \epsilon_{\rm eff}(\lambda))$. The total energy E_2 emitted from the dust grains is then given by

$$E_2 = R^2 A_{\rm total} \int_0^\infty B(\lambda, T_{\rm grain}) Q^{\rm abs}(\lambda, \epsilon_{\rm eff}(\lambda))\, {\rm d}\lambda, \qquad (3)$$

where R is the distance between the star and the dust grains.

In equilibrium, the energy balance $E_1 = E_2$ then enables the determination of the grain temperature $T_{\rm grain}$. We use the fixed values for R_* and R given in Table 2.

Having computed $T_{\rm grain}$ through the energy balance, we can now determine the SED for the dust grains through the standard relation between the flux F_λ and the Planck distribution at temperature $T_{\rm grain}$,

Table 2. Parameter values used in evaluating the energies E_1 and E_2 and the SED as in equation (4). These parameters are treated as constant here, and are set to values typical for circumstellar dust grains. The observer–grain distance is approximately 160 pc, the number of grains is similar to that in a protoplanetary disc of a few times the Minimum Mass Solar Nebula, the stellar radius and surface temperature are those of the Sun, and the star–grain distance is 50 au, similar to the radius of the Sun's Kuiper Belt.

Parameter	Value	Units	Meaning
$D_{\rm obs}$	5×10^{18}	m	Observer–dust grain distance
$N_{\rm g}$	10^{34}		Number of dust grains
R_*	7×10^8	m	Stellar radius
T_*	6000	K	Stellar surface temperature
R	7.5×10^{12}	m	Star–dust grain distance

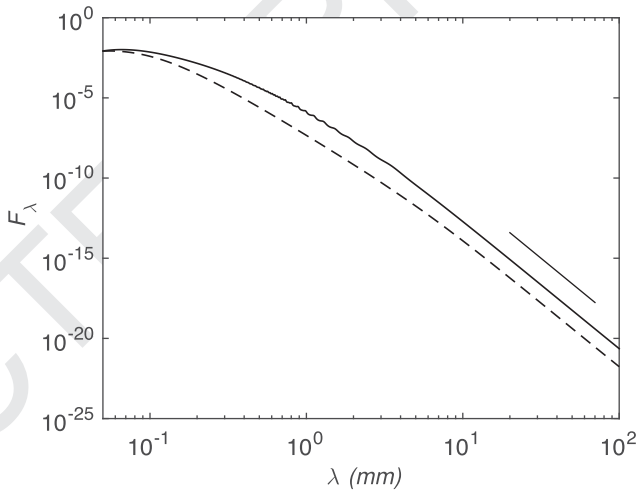

Figure 3. SEDs for clusters of silicate monomers of equal total volumes $V = 4\pi/3 \times 10^{-9}$ m^3, for volume fractions $f = 0.1$ (lower curve, dashed line) and $f = 0.3$ (upper curve, solid line). The flux F_λ is computed using the parameters in Table 2, and we set the size of the individual monomers $\delta = 10^{-7}$ m. The slope bar in the lower right-hand side indicates an exponent of -8. The y-axis units in this and subsequent SED plots are W m^{-2} m^{-1}.

i.e.

$$F_\lambda = \frac{N_{\rm g}}{D_{\rm obs}^2}\, A_{\rm eff}\, Q^{\rm abs}(\lambda)\, B(\lambda, T_{\rm grain}), \qquad (4)$$

where $N_{\rm g}$ is the observed number of dust grains and $D_{\rm obs}$ is the distance from dust grain to observer; these are purely scalefactors and do not affect the *shape* of the distribution F_λ, which is our primary interest. Different models for the material composition of dust grains will change $T_{\rm grain}$ and F_λ since both E_2 and equation (4) depend on the quality parameter $Q^{\rm abs}(\lambda)$, which depends on the dielectric coefficient of the material. Similarly, different geometric assumptions change $T_{\rm grain}$ and F_λ through the surface areas for absorption $A_{\rm eff}$ and emission $A_{\rm total}$, as well as the absorption coefficient $\mathcal{A}$.

3 RESULTS

3.1 Clustered aggregates of silicate monomers

Recall that the geometry of the clusters depends on two parameters: the size δ of individual spheres within the cluster and the volume fraction f of solid inclusions. Fig. 3 shows illustrative results of our

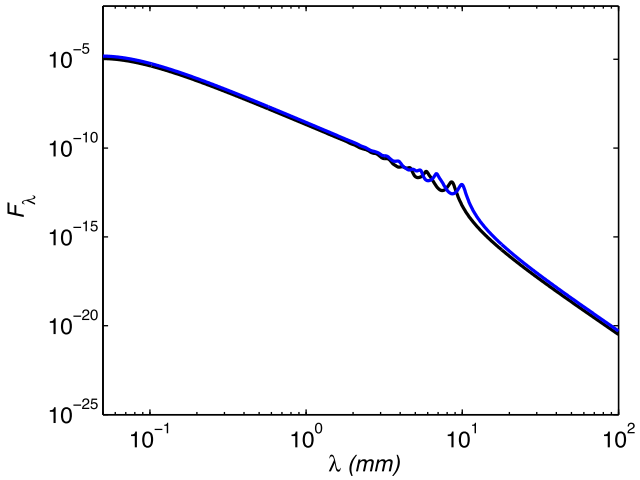

Figure 4. SEDs for compacted grains consisting of a silicate matrix with inclusions of FeS occupying a volume fraction $f = 0.1$. Results for two different grain sizes are shown: radii 1 (black) and 1.16 mm (blue).

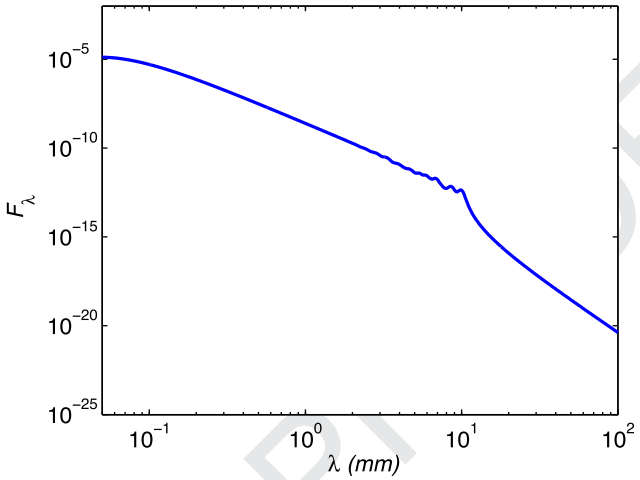

Figure 5. Smoothed and averaged SEDs for compacted grains consisting of a silicate matrix with inclusions of FeS occupying a volume fraction $f = 0.1$. The curves in Fig. 4 were averaged together before a smoothing filter was applied to the averaged SED.

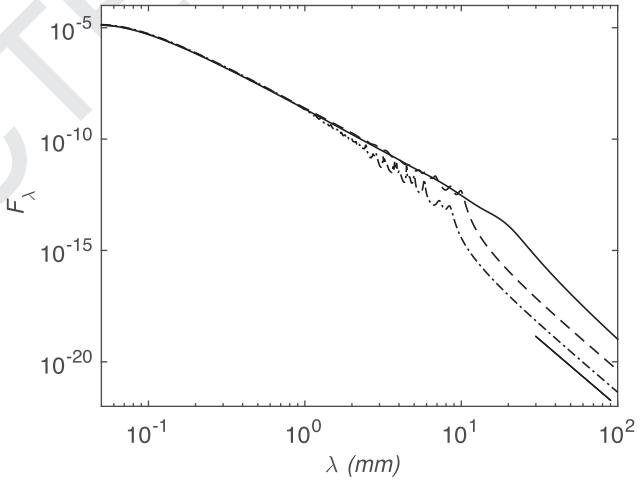

Figure 6. Smoothed and averaged SEDs for compacted grains consisting of a silicate matrix with inclusions of FeS occupying volume fractions of $f = 0$ (lower curve, dot–dashed line), $f = 0.1$ (middle curve, dashed line, as shown in Fig. 5) and $f = 0.3$ (upper curve, solid line). The slope bar in the lower right-hand side indicates an exponent of -6.

model for the case of a clustered aggregate of monomers, at two volume fractions $f = 0.1$ and $f = 0.3$, holding $\delta = 10^{-7}$ m constant.

The temperature $T_{\rm grain}$ of the dust grains does not vary significantly with f: At $f = 0.1$, we find $T_{\rm grain} = 52.5$ K, while at $f = 0.3$, we find $T_{\rm grain} = 44.5$ K. As one might expect, the flux increases with increasing f. More interestingly, the lower curve ($f = 0.1$) is flatter in the range of $0.1 < \lambda < 3$ mm. SEDs for more extreme values of f down to $f = 10^{-2}$ do not reveal any changes in the shape of the SED, other than an increase in the grain temperature and consequent shift of the maximum of the curve to shorter wavelengths. Higher values of f become problematic as we would then violate modelling assumptions made in Section 2.

3.2 Compacted object with inclusions

The compacted case consists of spherical grains of radius 1 mm, which contain sparsely distributed (spherical) inclusions of iron sulphide. Since in this case we assume solid convex dust grains, the Cauchy result holds, i.e. $A_{\rm eff}/A_{\rm total} = 1/4$, as described in Section 2.1.2. However, the mixture of silicate and FeS complicates the absorption factor $\mathcal{A}$ and the effective dielectric constant due to the differing dependences of the two component dielectric constants on wavelength. Fig. 4 compares the SED for compacted aggregates containing a volume fraction $f = 0.1$ of FeS inclusions, for two slightly different sizes of grain, having radii 1 and 1.16 mm. The effect of the interaction between the grain size and the wavelengths of the emitted photons gives rise to small amplitude oscillations in the curves, although the overall shapes of the two curves are extremely similar. The results for two different radii indicate that the oscillations are a fine detail that is unlikely to be observable in astronomical data, since a typical dust disc will contain a range of sizes of grains. These two radii were accordingly selected so that the small amplitude oscillations visible in the curves were in antiphase.

In order to generate an SED that is more typical of what might be observed, we further manipulate the model results by first averaging over the two grain sizes, and then applying a smoothing filter to the data, more closely to mimic what is achievable from real observing. The SED that results from this averaged, smoothed procedure is shown in Fig. 5. Notice that the amplitude of the oscillations has been substantially reduced, but that there is still a reasonably sharp change in slope at a wavelength an order of magnitude larger than the dust grain radii used.

Fig. 6 compares the SEDs obtained from two different volume fractions of FeS: $f = 0.1$ and $f = 0.3$, together with the SED obtained for a zero volume fraction of FeS, i.e. solid silicate grains. We observe that as the volume fraction of FeS increases, the temperature of the grains increases very slightly; for $f = 0.1$, we find $T = 60.6$ K, and for $f = 0.3$, we find $T = 61.3$ K. As f increases, the flux F_λ increases at wavelengths longwards of a centimetre, and the downturn in the slope occurs at larger λ for larger f. At low f, the curves can be described as having a convex bend; the convex bend at $\lambda \approx 10$ mm becomes less pronounced as f increases towards 0.3. A distinct knee persists at all f, different from the smooth variation in slope for silicate clusters, as shown in Fig. 3.

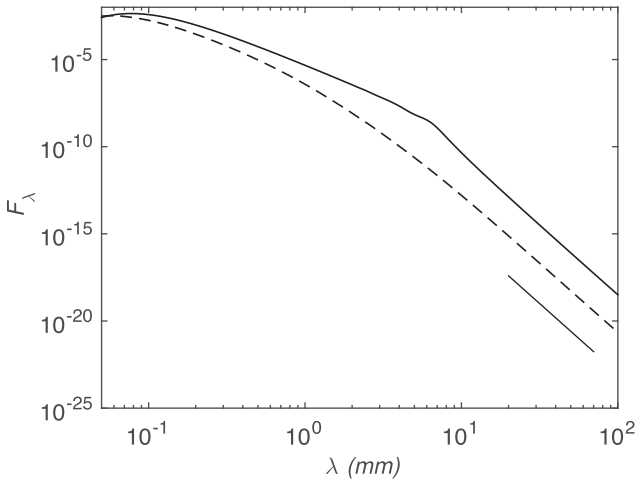

Figure 7. SEDs for clustered aggregates consisting of FeS monomers with no silicate, occupying volume fractions of $f = 0.1$ (lower curve, dashed line) and $f = 0.3$ (upper curve, solid line). The slope bar in the lower right indicates an exponent of -8.

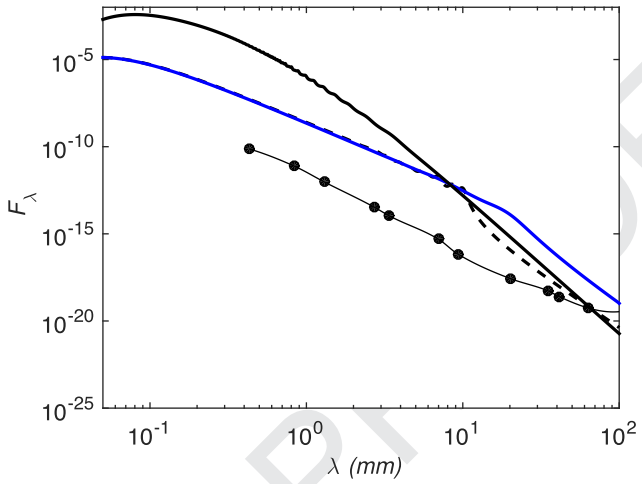

Figure 8. Observational data of fluxes F_λ. The data are from (in order of increasing wavelength) Qi et al. (2006); Qi, Öberg & Wilner (2013); Wilner et al. (2001, 2003, 2000); Menu et al. (2014); Claussen & Wilner (2001); and Wilner et al. (2005). For clarity, measurements at very similar wavelengths were averaged, and error bars (generally smaller than symbol sizes) are omitted. The overplotted curves are the model SEDs for $f = 0.3$ clusters (solid black line) and for compacted grains with $f = 0.1$ (dashed line) and $f = 0.3$ (solid blue line). The observational data are interpolated by piecewise cubic Hermite polynomials.

3.3 Clustered aggregates of solid FeS monomers

Finally, for comparison we compute the SEDs for the case of purely FeS monomers in the clustered aggregate geometry of Section 3.1, i.e. replacing the small astronomical silicate monomers with FeS. The results are shown in Fig. 7 for the cases of volume fractions $f = 0.1$ (temperature $T = 51.0$ K) and $f = 0.3$ (temperature $T = 37.9$ K). Comparing Figs 3 and 7, a knee appears (at $f = 0.3$) only when the monomer material is FeS. Comparing also to Fig 6, a similar knee is seen at $f = 0.3$ when FeS is incorporated in the silicate matrix (aggregate). Thus, it appears to be the FeS properties that produce the knee, rather than the nature of the matrix. The value of f alters how pronounced the changes of slope in the SED are, around 10 mm. However, at long wavelengths, it is interesting to compare the tail exponents in the three cases. For the two cases of clustered aggregates (Figs 3 and 7), the exponents of the SED at large λ are close to -8, as indicated in the figures. For the case of compacted grains, the exponent is much closer to -6; in all cases, these exponents appear to depend only weakly on f.

Silsbee & Draine (2016) have recently looked at the arguments for iron-bearing monomers in fluffy aggregates, to address the nature of interstellar particles captured by the *Stardust* mission (Sokolsky et al. (2008). However, they concluded that these postulated aggregates do not in fact solve the problem of the decelerations observed. Hence, they may not be a realistic case for the SEDs of circumstellar discs examined here.

4 COMPARISON WITH OBSERVATIONAL DATA

To test the above models, an observed disc needs to fulfil as many as possible of the model assumptions. In particular, the dust emission should be optically thin, and arise from particles at a single temperature. The latter strictly requires grains of one size and one star–particle distance; otherwise, the thermal balance with stellar heating produces a range of temperatures. To be useful, the data also need to span a couple of decades in wavelength, in the far-infrared to radio regime, where the SEDs change in slope. These requirements will conflict, to some extent, as well-studied discs tend to be those that are bright, and brightness is boosted for dust with moderate optical depth and spread over a range of star–particle distances. Finally, there needs to be a usable diagnostic output of the model; for example, temperature changes alone are insufficient as these cannot be verified through independent experiment. We emphasize that the model developed above should not blindly be applied to discs that do not fulfil, at least approximately, these criteria.

We use here a compilation of flux measurements for the disc around TW Hydrae, spanning the submillimetre to radio wavelength regimes. The data are very complete and of a good signal-to-noise ratio, which allows us to test details of our SED models, but the single star–particle distance approximation is not ideal. Nomura et al. (2016) place most of the millimetre-emitting dust at between 10 and 40 au from the star, for example. A positive consideration for choosing this system is that, at around 10 Myr, it is relatively old, and so has only a weak ionized wind. This reduces the radio emission of free–free transitions of electrons, which Menu et al. (2014) find to contribute significantly only at the longest wavelength shown here, of 6 cm.

Fig. 8 shows the SED of TW Hya overplotted with three example models. We do not attempt here to make any close quantitative match of the model assumptions to this particular disc. Absolute fluxes will be affected by the disc mass, which Menu et al. (2014) estimate at three times less than our model equivalent, and the distance to the star, which is 3.5 times closer than our nominal value. The SED decline is strongly affected by the distribution of grain sizes (e.g. Greaves et al. 2012), so this is also not matched in our demonstration models where all the grains have a dimension of 1 mm. It is the local structure within the SED that we examine here.

The TW Hya data show a knee and convexity around 10 mm wavelengths, features which are similar to the compacted grain with FeS inclusions. This is the only case of this type in our models. The slope of the TW Hya SED at the longest wavelengths is approximately -3.5, which is considerably shallower than in any of the models, but a range of grain sizes or temperatures would contribute to this; we leave additional investigation to be the subject

of future work. The wavelength where the observed flux drops is slightly shortwards of the model result, so a representative particle size just under 1 mm would probably give better agreement. We have not attempted to fine-tune the model developed here in order to fit the TW Hya data optimally.

That the case that best matched the TW Hya data is the compacted aggregate case was not expected a priori. For TW Hya, the extent of the dust disc is nearly as large as the Sun's Kuiper belt of comets, so fluffy cometary clusters might have been a natural expectation. While Menu et al. (2014) found signatures of iron-bearing olivines in the TW Hya disc, there are no data on the possible presence of iron inclusions.

With these caveats, it is encouraging that our simple models reproduce features of the data. In particular, the initial aim to produce diagnostics of grain composition and structure has succeeded. The model SEDs produce changes of slope at long wavelengths, with differing local behaviours, which are distinct for dust grains of cometary and asteroidal types.

5 CONCLUSIONS

In this paper, we have proposed, and investigated the consequences of, a simple model for the SED produced by variations in the geometry and composition of dust grains. Our major conclusions are as follows: (i) In the silicate cluster case, the model produces a smoothly varying SED with no obvious structure, and in the FeS cluster case, a knee appears at a sufficiently large volume fraction $f \approx 0.3$. (ii) In the compacted aggregate case, there is always a knee, and a convex bend also appears at a low volume fraction of FeS inclusions.

Comparing the model results to the SED of the TW Hya dust disc (which does fall into approximately the regime where our model assumptions are valid), similarities are found with the predictions of compacted grains with inclusions. For the dust lying at tens of au from TW Hya, the composition appears to be different from that in the analogous belt in the Solar system, where the dust is cometary in nature.

Future work will consider how the size distributions associated with the growth and break-up of comets and asteroids influence these results. Preliminary tests for TW Hya, using the code of Greaves et al. (2012), show that knee effects in the SED persist even for a range of grain temperatures and sizes; this is predominantly because the largest grains present control the downturn in the SED slope where $x < 1$. The present approach could also be extended reasonably straightforwardly to consider grains that collect ice mantles, in the cold outer regions of circumstellar discs.

ACKNOWLEDGEMENTS

We are very grateful to the referee for substantial remarks that have significantly improved this paper. JHPD gratefully acknowledges the support of the Royal Society through a University Research Fellowship. JSG thanks the University of St Andrews for research leave support.

REFERENCES

Birnstiel T., Dullemond C. P., Pinilla P., 2013, A&A, 550, L8
Blum J., 2010, Res. Astron. Astrophys., 10, 1199
Bohren C. F., Huffman D. R., 1983, Absorption and Scattering of Light by Small Particles. Wiley, New York
Booth M., Wyatt M. C., Morbidelli A., Moro-Martin A., Levison H. F., 2009, MNRAS, 399, 385
Claussen M. J., Wilner D. J., 2001, BAAS, 33, 1435
Cuzzi J. N., Estrada P. E., Davis S. S., 2014, ApJS, 210, 21
de Val-Borro M. et al., 2014, A&A, 564, 124
Dohnanyi J. S., 1968, in Kresak L., Millman P.M. eds, Proc. IAU Symp. 33, Physicas and Dynamics of Meteors. p. 486
Draine B. T., Lee H. M., 1984, ApJ, 285, 89
Duprat J., Engrand C., Maurette M., Kurat G., Gounelle M., Hammer C., 2007, Adv. Space Res., 39, 605
Greaves J. S., Hales A. S., Mason B. S., Matthews B. C., 2012, MNRAS, 423, L70
Henning T., Mutschke H., 1997, A&A, 327, 743
Henning T., Pfau W., Zinnecker H., Prusti T., 1993, A&A, 276, 126
Hildebrand R. H., 1983, Q. J. R. Astron. Soc., 24, 267
Hofmeister A. M., Keppel E., Speck A. K., 2003, MNRAS, 345, 16
Köhler M., Jones A., Ysard N., 2014, A&A, 565, L9
Lisse C. M. et al., 2012, ApJ, 747, 93
Menu J. et al., 2014, A&A, 564, A93
Min M., Waters L. B. F. M., de Koter A., Hovenier J. W., Keller L. P., Markwick-Kemper F., 2007, A&A, 462, 667
Min M., Rab C., Dominik C., Woitke P., 2013, Protostars and Planets VI. Heidelberg, July 15–20, 2013. Poster # 2S044
Niimi R. et al., 2012, ApJ, 744, 18
Nomura H. et al., 2016 ApJ, 819, L7
Ormel C. W., Okuzumi S, 2013, ApJ, 771, 44
Pérez L. et al., 2012, ApJ, 760, L17
Pollack J. B., Hollenbach D., Beckwith S., Simonelli D. P., Roush T., Fong W., 1994, ApJ, 421, 615
Qi C., Wilner D. J., Calvet N., Bourke T. L., Blake G. A., Hogerheijde M. R., Ho P. T. P., Bergin E., 2006, ApJ, 636, L157
Qi C., Öberg K. I., Wilner D. J., 2013, ApJ, 765, 34
Shen Y., Draine B. T., Johnson E. T., 2008, ApJ, 689, 260
Sheret I., Dent W. R. F., Wyatt M. C., 2004, MNRAS, 348, 1282
Silsbee K., Draine B. T., 2016, ApJ, 813, 133
Wilner D. J., 2001, in Jayawardhana R., Greene T., eds, ASP Conf. Ser. Vol 244, Young Stars Near Earth: Progress and Prospects. Astron. Soc. Pac., San Francisco, p. 191
Wilner D. J., Ho P. T. P., Kastner J. H., Rodríguez L. F., 2000, ApJ, 534, L101
Wilner D. J., Bourke T. L., Wright C. M., Jørgensen J. K., van Dishoeck E. F., Wong T., 2003, ApJ, 596, 597
Wilner D. J., D'Alessio P., Calvet N., Claussen M. J., Hartmann L., 2005, ApJ, 626, L109
Winston E. et al., 2012, A&A, 545, 145
Woitke P. et al., 2016, A&A, 586, A103
Wyatt M. C., Dent W. R.F, 2002, MNRAS, 334, 589
Yamamoto S., Mukai T., 1998, Earth Planets Space, 50, 531
Zolensky M. et al., 2008, Meteorit. Planet. Sci., 43, 261

This paper has been typeset from a TEX/LATEX file prepared by the author.

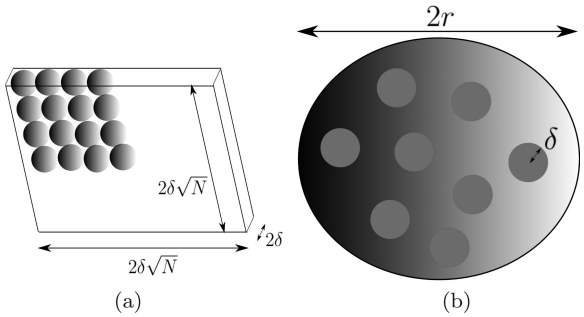

Figure 1. Two possible idealized geometries for dust grains. (a) A clustered aggregate formed from $N \gg 1$ monomers of radius δ producing a cluster of length-scale $r \gg \delta$. (b) A 'compacted' composite grain model: a large silicate grain of radius r containing inclusions of radius $\delta \ll r$ consisting of iron sulphide.

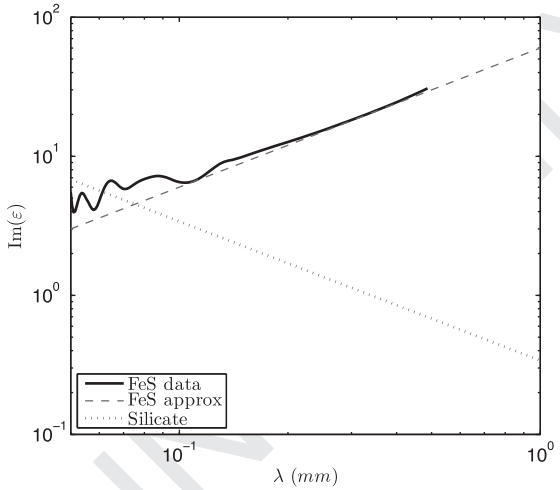

Figure 2. Experimental data for the imaginary part of the dielectric coefficient Im(ϵ) for iron sulphide FeS (black solid line), from Henning & Mutschke (1997), together with the approximation (red dashed line) $\mathrm{Im}(\epsilon_{\mathrm{FeS}}) = 6.0 \times 10^4 \lambda$ (where λ is measured in metres). We also show the dependence on λ of the imaginary part of the dielectric coefficient for astronomical silicate $\mathrm{Im}(\epsilon_{\mathrm{sil}})$; see equation (2).

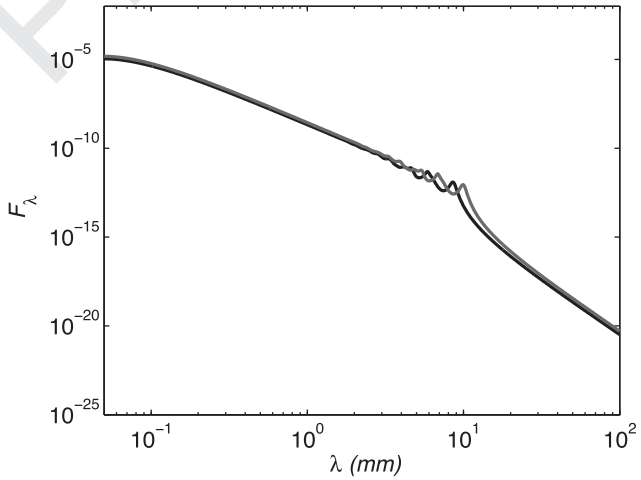

Figure 4. SEDs for compacted grains consisting of a silicate matrix with inclusions of FeS occupying a volume fraction $f = 0.1$. Results for two different grain sizes are shown: radii 1 (black) and 1.16 mm (blue).

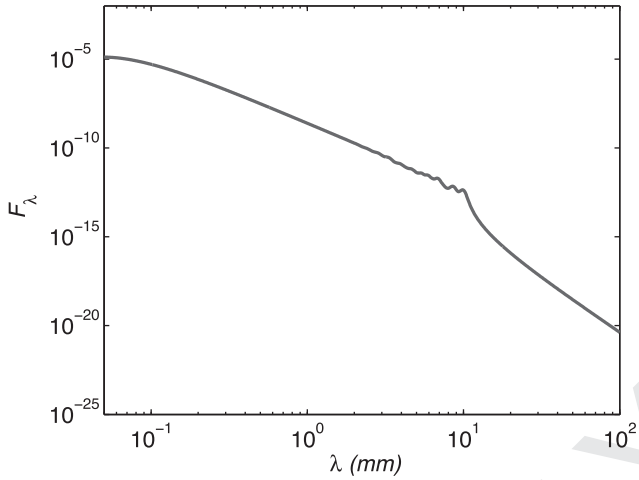

Figure 5. Smoothed and averaged SEDs for compacted grains consisting of a silicate matrix with inclusions of FeS occupying a volume fraction $f = 0.1$. The curves in Fig. 4 were averaged together before a smoothing filter was applied to the averaged SED.

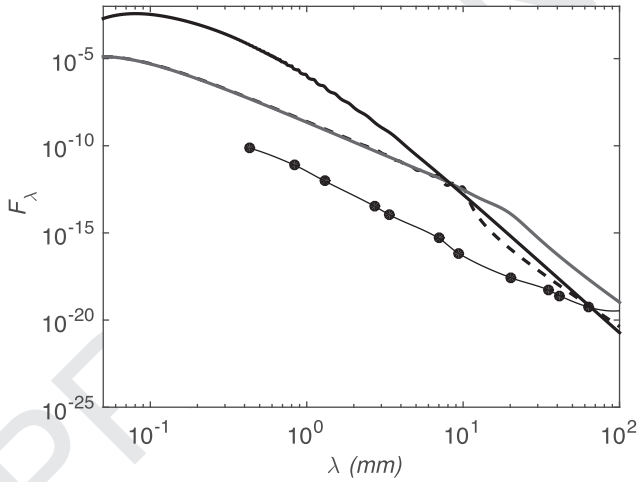

Figure 8. Observational data of fluxes F_λ. The data are from (in order of increasing wavelength) Qi et al. (2006); Qi, Öberg & Wilner (2013); Wilner et al. (2001, 2003, 2000); Menu et al. (2014); Claussen & Wilner (2001); and Wilner et al. (2005). For clarity, measurements at very similar wavelengths were averaged, and error bars (generally smaller than symbol sizes) are omitted. The overplotted curves are the model SEDs for $f = 0.3$ clusters (solid black line) and for compacted grains with $f = 0.1$ (dashed line) and $f = 0.3$ (solid blue line). The observational data are interpolated by piecewise cubic Hermite polynomials.